

Photocatalytic activity enhancement by addition of lanthanum into the BiFeO₃ structure and the effect of synthesis method

*Hamed Maleki**

Faculty of Physics, Shahid Bahonar University of Kerman, Kerman, Iran

e-mail address: hamed.maleki@uk.ac.ir

Keywords: Photocatalytic properties; Multiferroics; optical bandgap, sol-gel; Lanthanum doped; hydrothermal.

Abstract: In this paper, the photocatalytic activity of multiferroics BiFeO₃ (BFO) and Bi_{0.8}La_{0.2}FeO₃ (BLFO) nanocrystals with two different morphologies which were synthesized by two different sol-gel (SG) and hydrothermal (HT) methods have been studied. All the obtained samples were characterized using X-ray diffractometer, Fourier transform infrared spectroscopy, transmission electron microscopy, UV-vis spectroscopy and vibrating sample magnetometer. Differential thermal analysis (DTA) measurements were probed ferroelectric-paraelectric first-order phase transition (T_C) for all samples. Addition of lanthanum decreases the electric phase transition. For photocatalyst application of bismuth ferrite, adsorption potential of nanoparticles for methylene blue (MB) organic dye was evaluated. The doping of La in the BFO structure enhanced the photocatalytic activity and about 71% degradation of MB dye was obtained under visible irradiation. The magnetic and ferroelectric properties of BLFO nanoparticles improve compared to the undoped BiFeO₃ nanoparticles. The non-saturation at high applied magnetic field for as-prepared samples by HT is related to the size and shape of products. This work not only presents an effect of lanthanum substitution into the bismuth ferrite structure on the physical properties of BFO, but also compares the synthesis method and its influence on the photocatalytic activity and multiferroics properties of all nanopowders.

1. Introduction

In order to generate hydrogen, an environmentally friendly process has been offered to modern society through photocatalytic degradation of pollutants and photocatalytic water

splitting using solar energy [1–3]. Multiferroic materials have recently drawn scientist’s attention due to their vast applications as a result of their photocatalysis and photovoltaics properties. The narrow energy band gap and ferroelectric properties lead to high absorption of light in the visible region [4–7]. Bismuth ferrite, which simultaneously shows ferroelectric and ferromagnetic behavior at and above room temperature (RT), has drawn attention for two decades. This increasing interest in bismuth ferrite as a noble material is due to its potential application in multifunctional devices, data storage, sensors and photovoltaic technologies [8–18]. This matter has the anti(ferro)-magnetic to paramagnetic transition at Neel temperature $T_N \sim 370^\circ\text{C}$ and ferroelectric-paraelectric first order phase transition at Curie temperature $T_C \sim 830^\circ\text{C}$ [19–23].

Literature survey indicates that, with periodicity of 62 nm spin structure in BFO gives a spiral modulation and is a cause of G-type antiferromagnetic ordering of bulk bismuth ferrite [24–26]. Moreover, due to the formation of secondary phase and impurities during synthesis process, BFO has large leakage current density (because of various oxidation states of Fe ion and the existence of oxygen vacancies) [8,27–29]. Many theoretical and experimental studies of bismuth ferrite have been carried out to expand the applications and solve the problems hindering practical usage of BFO [30–32]. To overcome these obstacles, parallel to synthesis of BFO nanoparticles with different methods [11,33–35], it has been reported that A-site or B-site substitution into the structure of bismuth ferrite, is the most effective strategy to reduce the impurity phases and enhanced multiferroic properties [36–44].

Apart from these multiferroic properties of BiFeO_3 , according to the narrow band-gap of BFO (~ 2.2 eV), bismuth ferrite has been also known as a magnetic photocatalyst at visible light irradiation for water splitting and degradation of organic pollutants [5,7,45]. The weak ferromagnetic nature of BiFeO_3 nanoparticles is also used for recovering the catalyst from solution. However, the photocatalytic efficiency of bismuth ferrite is also limited as a result of its low conduction band (compared to H_2 or O_2) and small surface areas for catalytic reactions [1,46]. In order to enhance photocatalytic ability on the degradation of pollutants, BFO has been synthesized by varying its synthesis method and by varying its compositional parameters such as substitution.

To understand the origin of the influence of synthesis method, as well as the effect of addition of lanthanum into the structure of bismuth ferrite, we have synthesized BiFeO_3 and $\text{Bi}_{0.8}\text{La}_{0.2}\text{FeO}_3$ nanoceramics through the sol-gel and hydrothermal methods. The synthesis was

done to find a deep understanding about their effects on the multiferroic properties and photocatalytic activities of BiFeO₃ nanoparticles.

2. Experimental method

2.1 Sol-gel preparation of pure and La-doped BiFeO₃

BiFeO₃ and Bi_{0.8}La_{0.2}FeO₃ nanoceramics were synthesized via sol-gel (SG) process by using Bi(NO₃)₃.5H₂O, Fe(NO₃)₃.9H₂O and La(NO₃)₃.6H₂O (for the case of BLFO) as a starting materials, and deionized water and 2-methoxyethanole as a solvent [47,48]. Stoichiometric amount of bismuth, iron and lanthanum nitrate were completely dissolved in the solvent. Acetic acid was added to the above solution dropwise (pH~1.5) one hour later. A brownish and transparent sol is obtained after 1.5 h of constant stirring. Then the temperature was increased to 90°C and the solution was slowly evaporated and after 3h heating and stirring, the gel is obtained. The precursor powders were dried for 2h at 110°C and were calcined at 650°C for 3h. The as-prepared products synthesized through the sol-gel process were indexed SGBFO and SGBLFO for pure and La-doped bismuth ferrite respectively.

2.2 Hydrothermal synthesis of BFO and BLFO

In this method, for synthesis of BiFeO₃ (HTBFO) and Bi_{0.8}La_{0.2}FeO₃ (HTBLFO) samples, a stoichiometric amount of bismuth (III) nitrate pentahydrate (99%, Sigma), ferric (III) nitrate nonahydrate (99%, Merck) and lanthanum nitrate hexahydrate (99% Merck for HTBLFO) were dissolved in 10 ml of deionized water. Then 30 ml KOH (4M) was added to the solution dropwise under constant stirring. After 30 min stirring, the solution was transferred into a stainless Teflon-lined autoclave and heated at 220°C for 12h. Then the solution cooled naturally to the RT. The products were separated from the solution by centrifugation, then washed several times with distilled water and ethanol, and finally dried for 2 hours at 110 °C, in order to obtain brown nanopowders.

2.3 Characterization

First, the physical properties of pure and La-doped bismuth ferrite is studied. The crystallinity and structural properties of products were investigated by X-ray diffractometer (XRD) on a Philips X'pert, with Cu-K α radiation ($\lambda=1.54056 \text{ \AA}$) and Furrier transform inferared (FTIR) TENSOR27 spectrophotometer. The morphology and distribution of nanocrystals were observed by using transmission electron microscopy (TEM, Leo-912-AB). The thermal treatment and weight loss of the nanoparticles were recorded by differential thermal and thermal gravimetric analysis (TG-DTA, NETZSCH- PC Luxx 409) at a heating

rate of 10°C/min from RT up to 1000°C in air. The magnetic properties were measured by a Lake Shore (7410, SAIF) vibrating sample magnetometer (VSM) up to a maximum field of 20 kG. The optical properties of products were examined by UV-vis absorption spectra using Lambda900 spectrophotometer.

In the second part, the photocatalytic activity of all samples were evaluated by the degradation of methylene blue in aqueous solution using 300 W Xenon lamp under visible light irradiation. The starting concentration of MB was chosen 4 mg^l⁻¹ with dispersing 0.2g BFO or BLFO in aqueous solution of 200 ml. For achieving an adsorption equilibrium of MB on products surface, the aqueous suspension was stirred magnetically for a period of 75 min in the dark prior to irradiation. Then by turning on the lamp the changes of MB concentration were measured. Concentration variations were studied by measuring the absorbance of the solution at 664 nm using a UV-vis spectrophotometer. C/C_0 is known as the photocatalytic degradation ratio of MB, which has been investigated in this study. C_0 was the starting concentration of MB and C was the concentration of MB at time t .

3. Results and discussion

3.1 X-ray diffraction investigation

Fig. 1 shows the XRD patterns of BFO and BLFO nanoparticles prepared by sol-gel (Fig. 1 (a) and (b)) and hydrothermal (Fig. 1 (c) and (d)) methods. The recorded diffracted planes match well with the standard card of bismuth ferrite (JCPDS card No. 86-1518) and XRD patterns confirm the single perovskite phase of BiFeO₃ with distorted rhombohedral structure (R₃C). All patterns show strong and sharp diffraction peaks which indicate well crystallinity of all as-prepared particles. For pure BFO samples a few weak diffraction peaks related to the impurity phases like Bi₂Fe₄O₉ and Bi₂₅FeO₄₀ are observed. By adding La into the structure of BFO, these peaks are remained for HTBLFO sample, however for SGBLFO nanoparticles the impurity phases disappeared. For nanoparticles prepared by SG, dopant lanthanum changes the position of peaks a little to the smaller value and addition of La into the structure of bismuth ferrite, leads to a phase transformation from rhombohedral to monoclinic structure which is observed in the merging of two major peaks of BFO at 30<2θ<35 into the one peak (Figs.2 (b) and (d)) [47]. On the other hand, for HTBFO and HTBLFO nanoparticles, at a larger angle, the major peaks exhibit no phase transformation. The average crystallite size, has been obtained from the Scherrer formula $D = \frac{K\lambda}{\beta \cos\theta}$, where K is the shape factor that normally measures to be about 0.89, λ is the wavelength of Cu-K α radiation of the XRD, β is the width of the observed

diffraction peak at its half intensity maximum, and θ is the Bragg angle of each peak. The calculated average size for SGBFO and SGBLFO grains are 48 nm and 34 nm respectively.

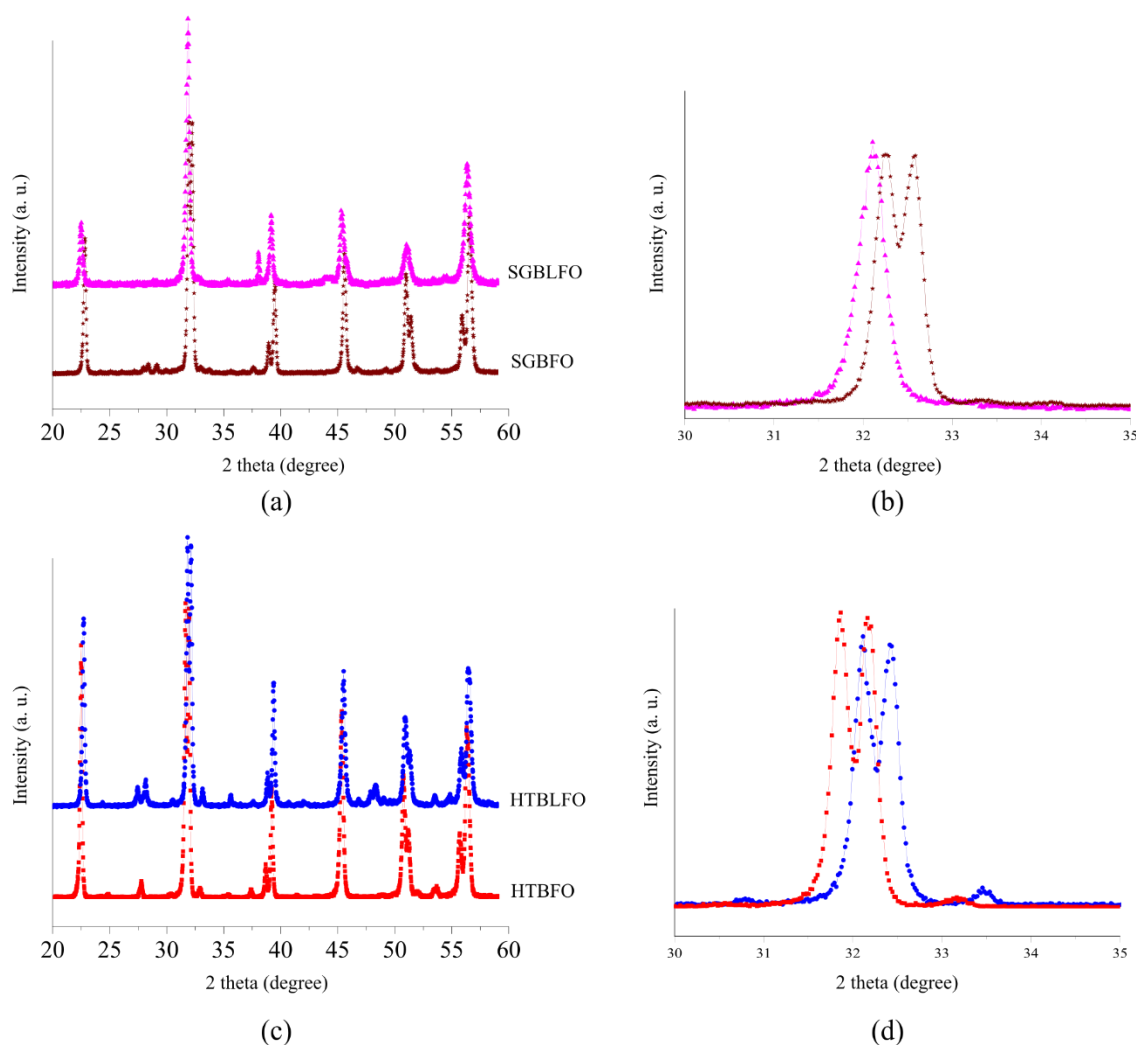


Fig. 1 (a) XRD patterns of BiFeO_3 and $\text{Bi}_{0.8}\text{La}_{0.2}\text{FeO}_3$ nanoparticles prepared by SG method, (b) same plot in the range of $30 < 2\theta < 35$, (c) XRD patterns of HTBFO and HTBLFO nanoparticles, (d) same graphs in the range of $30 < 2\theta < 35$.

3.2 Fourier transform infrared spectroscopy

To get further insight into the formation mechanism of BFO nanoparticles, the FTIR spectra of all samples were recorded. Fig. 2 illustrate the FTIR spectra of all as-synthesized nanoceramics in the wavenumber range of $400\text{-}4000\text{ cm}^{-1}$. Two major peaks between $400\text{-}600\text{ cm}^{-1}$ correspond to the Fe-O stretching and O-Fe-O bending vibrations of perovskite FeO_6 groups, which confirms the formation of BFO nanoparticles [11,49,50]. Between $1400\text{-}1650\text{ cm}^{-1}$ two peaks are observed which are related to the symmetry bending vibration of C-H or C-

H₂ [51]. The broad band at 3300-3700 cm⁻¹ is due to the symmetric and anti-symmetric stretching of H₂O and OH⁻ bond.

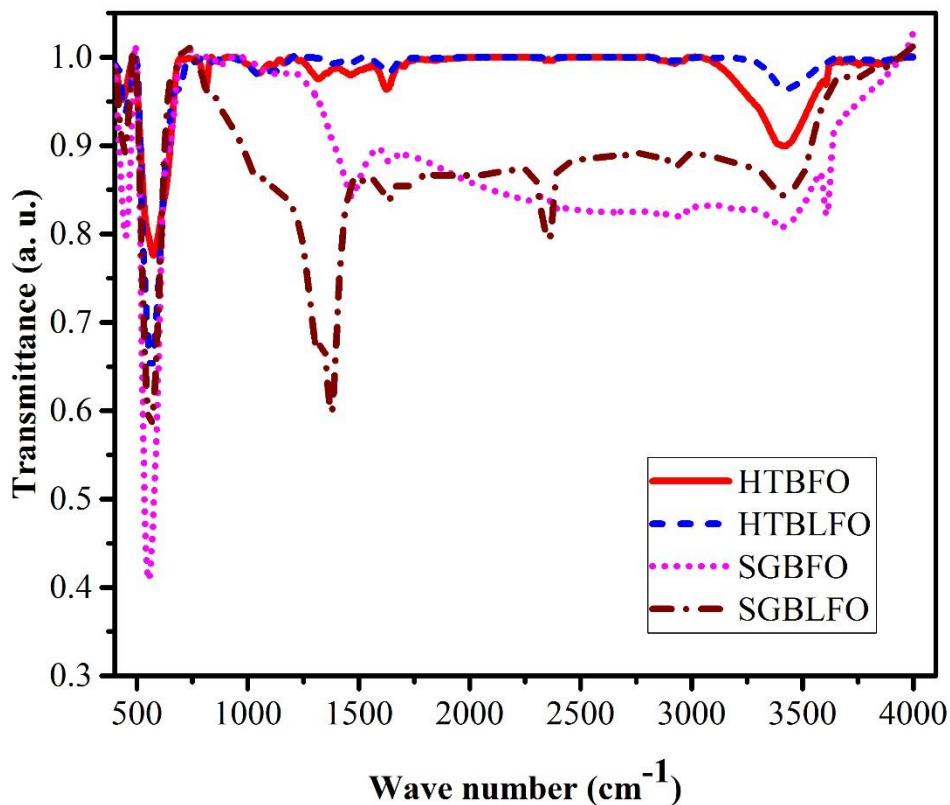


Fig. 2 FTIR spectra of BiFeO₃ and Bi_{0.8}La_{0.2}FeO₃ nanoparticles prepared by both SG and HT methods

3.3 Transmission electron microscope

TEM images of un-doped and La-doped BFO nanoparticles synthesized by SG and HT methods are presented in Fig. 3. The sol-gel as-prepared nanoparticles which are shown in Fig. 3 (a) and (b), have polyhedral morphology with the average size of 48 nm and 34 nm for SGBFO and SGBLFO nanoparticles respectively. TEM images of HTBFO and HTBLFO nanoceramics are illustrate in Fig. (c) and (d). The morphology of hydrothermal products are rod-like with diameters of ~52 nm (~43 nm) and length of less than 1μm for HTBFO (HTBLFO) nanoparticles. This morphological change via hydrothermal method, was strongly dependent on the synthesis process. It could be due to the nucleation rate of grains which is related to the condition of synthesis process. In both synthesis methods, The La concentration

had only a slight effect on the morphology and only reduced the size of grains, which is in agreement with the results from Scherrer formula.

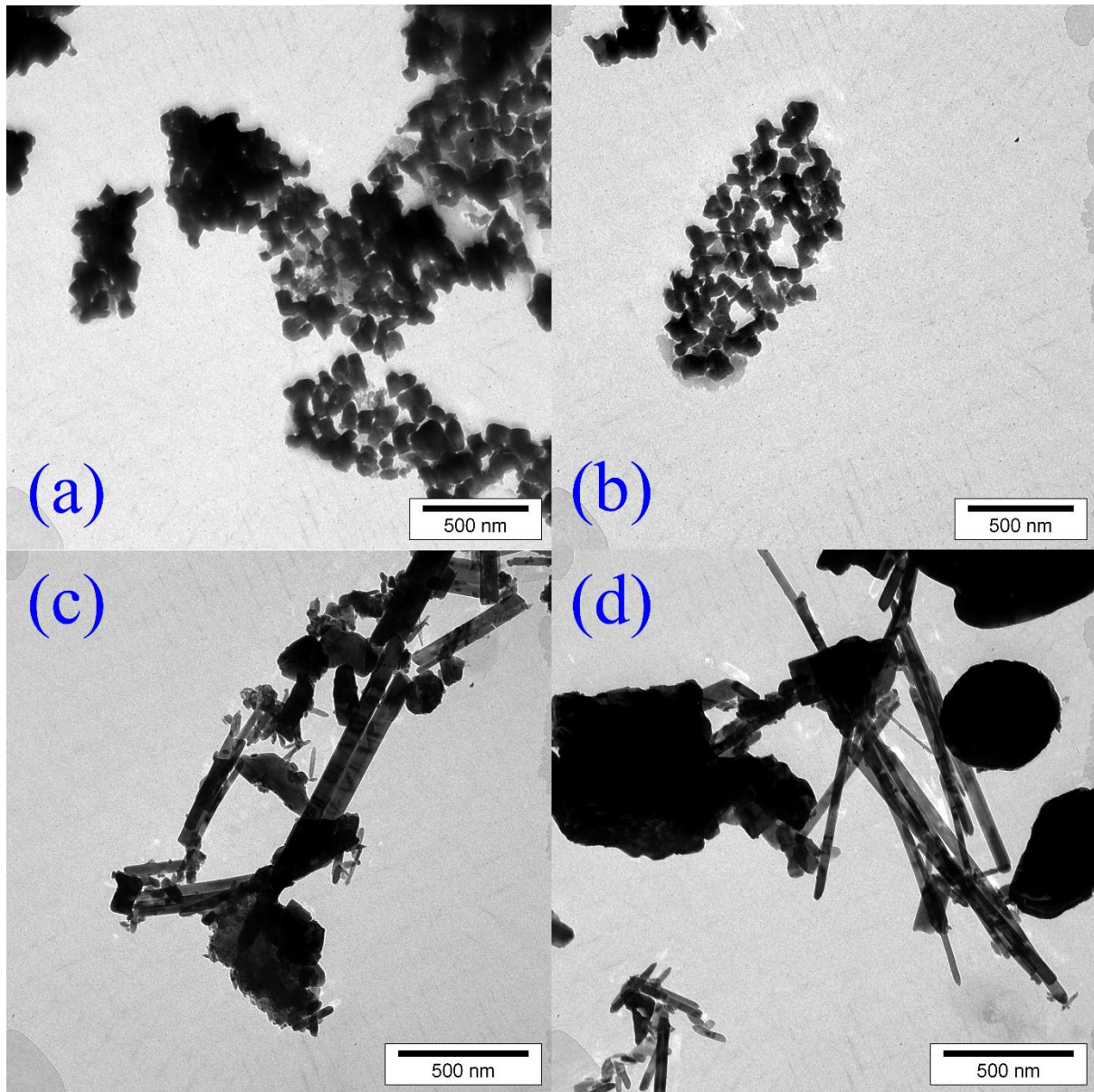


Fig. 3. TEM images of BiFeO_3 and $\text{Bi}_{0.8}\text{La}_{0.2}\text{FeO}_3$ synthesized by SG and HT methods, (a) image of SGBFO sample, (b) SGBLFO, (c) HTBFO and (d) HTBLFO

3.4 Thermal behavior

Fig. 4 shows the thermal gravitometric and differential thermal analysis (TG/DTA) curves of all products. In DTA curves, exothermic peaks are related to the crystallization and oxidation. On the other hand, phase transition and dehydration show endothermic peaks. TG curves of SGBFO and SGBLFO samples reveal the decomposition of the organic part of samples up to 400°C , with a wide exothermic peak on the DTA curves and $\sim 1.3\%$ of mass loss.

For the HTBFO (HTBLFO) samples (inset in Fig. 4 (b)), the total weight loss was 2.3% (1.5%) which is divided to three stages for HTBFO nanoparticles. First loss of 0.5% up to 300°C and then quick loss of 1% up to 390°C and finally 0.8% weight loss up to 700°C which is related to the complete decomposition of nanoparticles. When the lanthanum is added into the BFO structure, Curie temperature decreases from 830°C (827°C) for SGBFO (HTBFO) to 824°C (818°C) for SGBLFO (HTBLFO). The reason could be explained by lower polarizability of lanthanum ions in the structure of bismuth ferrite, compared to bismuth, as a result, the Curie temperature decreases [52].

3.5 M-H hysteresis loops analysis of BFO and BNLFO nanoceramics

The magnetic hysteresis loops of as-prepared samples were measured using VSM at RT with a maximum applied field of 20 KG (Fig.5). For all products a weak ferromagnetic behavior is observed. However HTBFO and HTBLFO nanoparticles didn't show a completed saturation magnetization. A significant enhancement in the value of saturation magnetization (M_s) on SG synthesis method is observed due to the smaller particle size and morphology. The M-H hysteresis loops data (Table 1), indicated that the remnant magnetization (M_r) and M_s decreases with addition of lanthanum. However the coercive forces increase. Dopant La and changes in the distribution of the bismuth and consequently iron ions in the A-site and B-site of BFO structure, changes the magnetic moments and anisotropy [16,26]

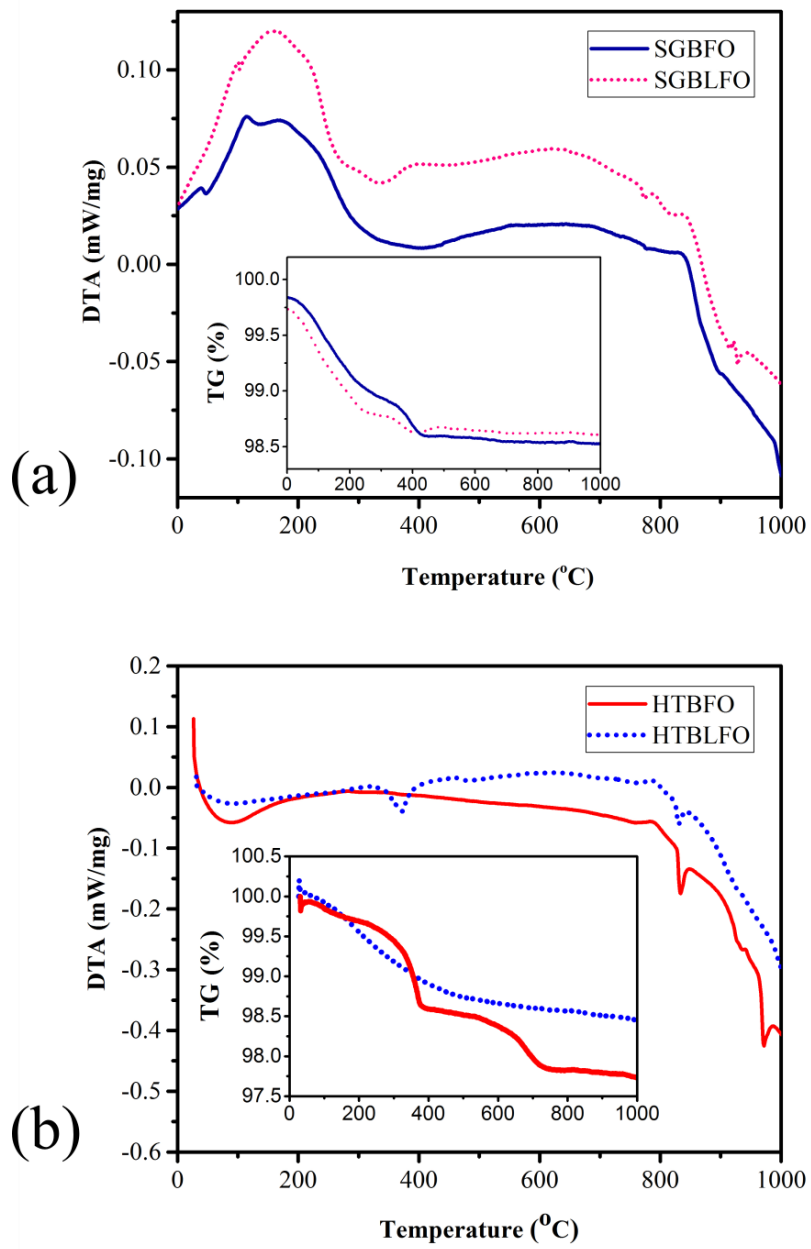


Fig. 4 (a) DTA curves of pure and 20%La-doped bismuth ferrite nanoparticles prepared by SG method. The inset shows the TG curves of products, (b) DTA and TGA (as inset) curves of HTBFO and HTBLFO nanorods.

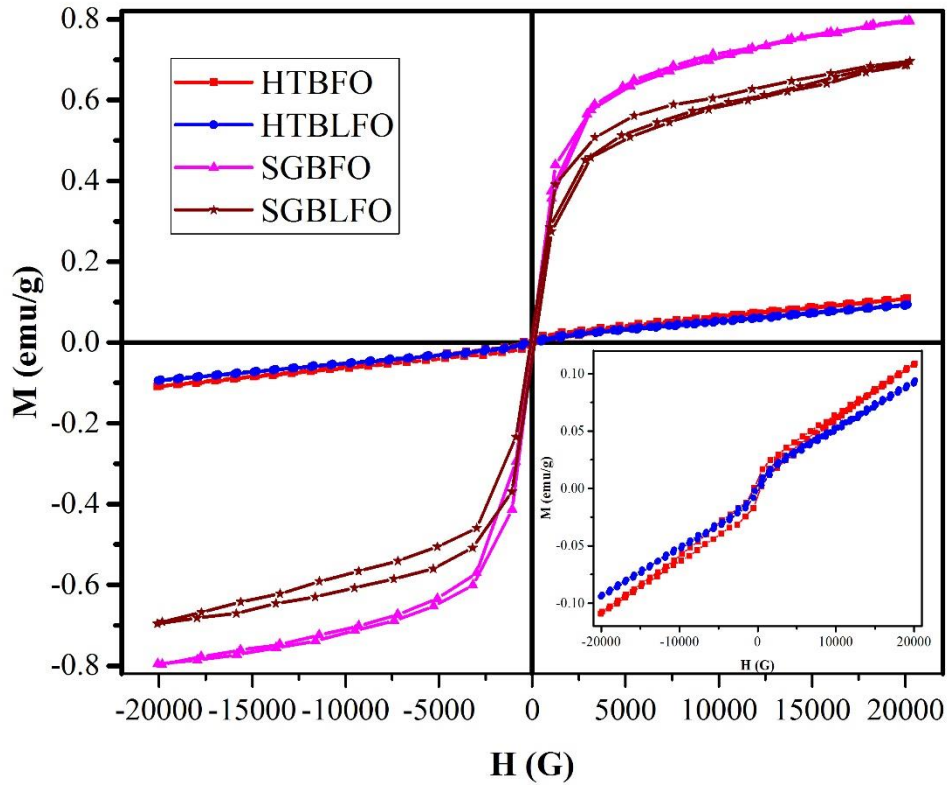


Fig. 5 M-H hysteresis loops of all as-prepared samples through SG and HT methods at RT. Inset shows hysteresis loops of BiFeO₃ and Bi_{0.8}La_{0.2}FeO₃ nanoparticles prepared by HT method separately

Table 1. The saturation and remanent magnetization, as well as coercivity of BFO and BLFO powders synthesized by SG and HT methods.

Sample	Sol gel			Hydrothermal		
	M _s (emu/g)	M _r (emu/g)	H _c (G)	M _s (emu/g)	M _r (emu/g)	H _c (G)
BiFeO ₃	0.797	15.596×10 ⁻³	39.034	0.109	7.077×10 ⁻³	383.653
Bi _{0.8} La _{0.2} FeO ₃	0.696	10.452×10 ⁻³	90.788	0.094	2.681×10 ⁻³	426.832

3.6 Uv-vis spectroscopy analysis

The optical spectra of as-prepared products as shown in Fig. 6 reveals a high absorption in the range of 500-600 nm for all samples. The direct optical band-gap energy of all nanoparticles was calculated using Tauc's equation $(\alpha h\nu)^2 = K(h\nu - E_g)$, where K is a constant, α is the absorption coefficient and $h\nu$ is the photon energy [53]. E_g is determined by plotting $(\alpha h\nu)^2$ vs

$h\nu$ and extrapolation of the straight line portion of the curves. The band gap decreases by La-substitution into the BFO structure. The optical band-gap was calculated 2.12eV (2.13 eV) for SGBLFO (HTBLFO) nanoparticles which was lower than pure BFO samples (2.16 eV for SGBFO and 2.17 eV for HTBFO).

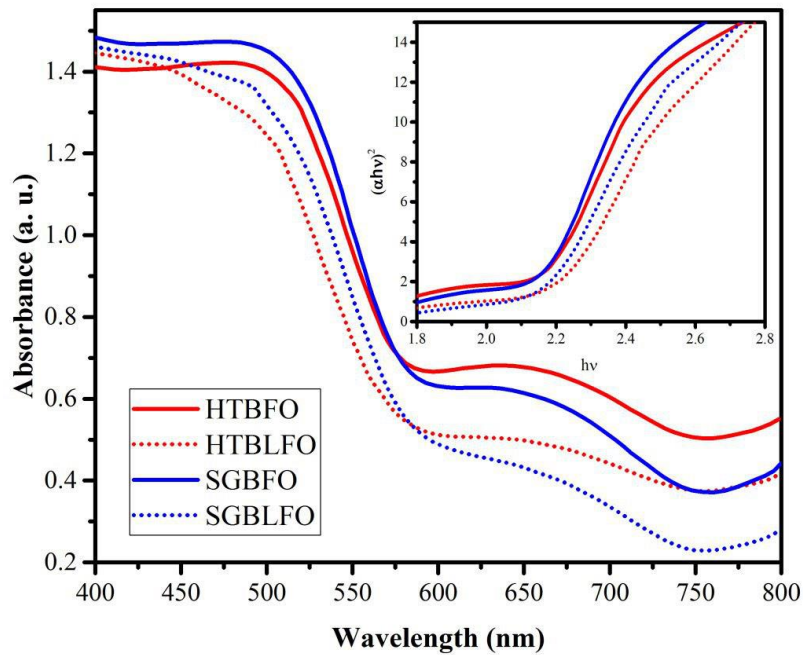


Fig. 6 UV-vis adsorption of of BiFeO_3 and $\text{Bi}_{0.8}\text{La}_{0.2}\text{FeO}_3$ nanoparticles prepared by both SG and HT methods

3.7 Photocatalytic activity of BFO and BNFO

The photocatalytic activity of BFO and BLFO nanoparticles is evaluated by the degradation of methylene blue (MB) under visible light irradiation. Herein, 0.2g sample was mixed by 4 mg/L of MB solution at RT. The photocatalytic degradation is measured from relation C/C_0 , where C and C_0 are concentration at time t and zero respectively considering the time unit minutes. Fig. 7 (a) shows the photo-gradation coefficients of all products vs. time. For SGBFO and HTBFO grains, 26% and 21% of degradation take place in 300 min. However 71% and 58% of degradation take place with SGBLFO and SGBFO nanocatalysts in 5h respectively. In principle, the efficiency of the photocatalysts depends on the factors like crystallite size, morphology, surface area, and band gap and photoinduced electron-hole separation efficiency of the catalyst. Fig. 7 (b) shows the rate constant of $\ln(C_0/C)$ vs. time. The rate constant k is calculated from the slopes of the fitted kinetics ($\ln(C/C_0) = -kt$) [54].

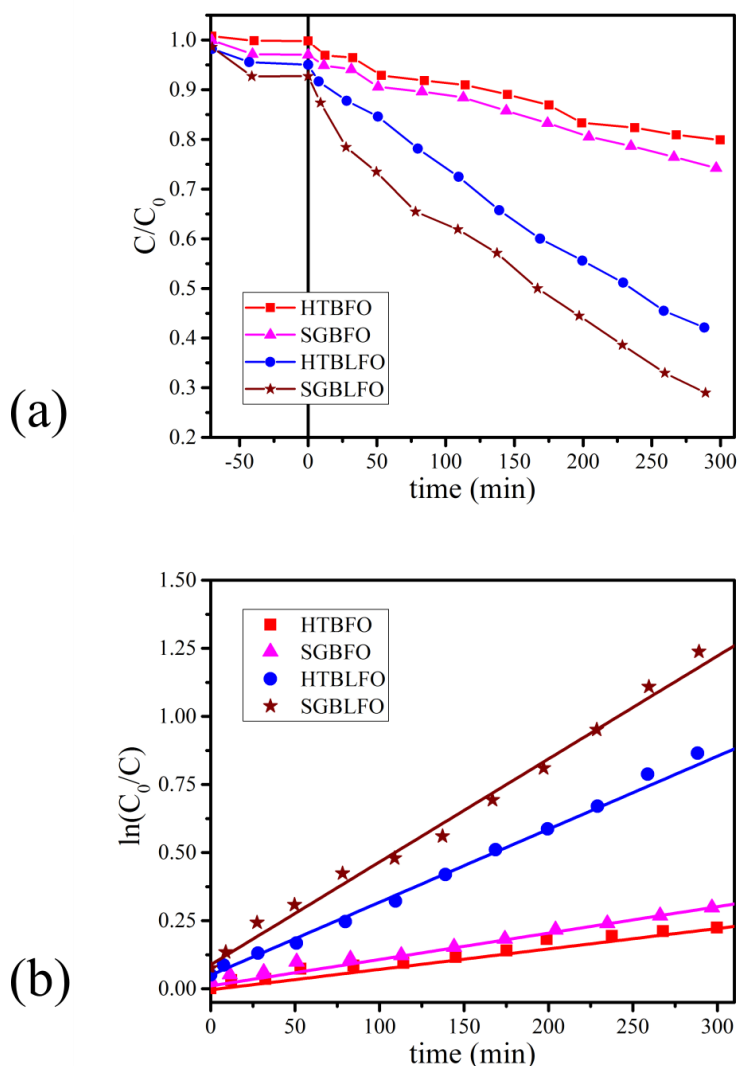


Fig. 7 (a) Degradation of MB solution in the presence of sol-gel and hydrothermal prepared BiFeO_3 and $\text{Bi}_{0.8}\text{La}_{0.2}\text{FeO}_3$ nanoparticles, (b) first order kinetics data for degradation of MB on SGBFO, SGBLFO, HTBFO and HTBLFO.

4. Conclusions

In summary, pure and La-doped BiFeO_3 nanoparticles were synthesized by two different sol-gel and hydrothermal methods. The effect of synthesis method, as well as, the enhancement of photocatalytic activity of bismuth ferrite nanoparticles by addition of lanthanum is investigated. XRD analysis confirms the rhombohedrally-distorted (R_3C) perovskite structure for all products. The TEM studies reveal that as-prepared nanoparticles synthesized by SG are semi-spherical powders. On the other hand, as-prepared samples

synthesized by HT have rod-like shape. DTA study indicated that addition of lanthanum in the Bi-site in the structure of BFO decreases the Curie temperature (T_C). Magnetic hysteresis loops showed the influence of synthesis method on the magnetic properties of samples. SGBFO and SGBLFO samples have much higher saturated magnetization which could be related to destruction of the spin cycloid magnetic ordering structure compared to rod-like HTBFO and BLFO nanoparticles. The photocatalytic reactivity of all samples was evaluated in terms of the degradation of MB in aqueous BFO and BLFO suspensions under visible light irradiation. The results indicated that the photocatalytic activity of products depends not only on the synthesis method but also on the addition lanthanum into the structure of bismuth ferrite.

Acknowledgments

This work was supported by the research council of Shahid Bahonar University of Kerman (SBUK-RC). Partial financial support by Iranian nanotechnology initiative council (INIC) are acknowledged.

5. References

- M. Humayun, A. Zada, Z. Li, M. Xie, X. Zhang, Y. Qu, F. Raziq, L. Jing, Applied Catalysis B: Environmental 180 (2016) 219. [1]
- Y. Wu, W. Han, S.X. Zhou, M.V. Lototsky, J.K. Solberg, V.A. Yartys, Journal of Alloys and Compounds 466(1–2) (2008) 176. [2]
- S. Wang, D. Chen, F. Niu, N. Zhang, L. Qin, Y. Huang, Journal of Alloys and Compounds 688 (2016) 399. [3]
- C.M. Cho, J.H. Noh, I.-S. Cho, J.-S. An, K.S. Hong, J.Y. Kim, Journal of the American Ceramic Society 91(11) (2008) 3753. [4]
- F. Gao, X.Y. Chen, K.B. Yin, S. Dong, Z.F. Ren, F. Yuan, T. Yu, Z.G. Zou, J.-M. Liu, Advanced Materials 19(19) (2007) 2889. [5]
- Y.-L. Pei, C. Zhang, Journal of Alloys and Compounds 570 (2013) 57. [6]
- H. Maleki, Journal of Magnetism and Magnetic Materials 458 (2018) 277. [7]
- J. Wang, J.B. Neaton, H. Zheng, V. Nagarajan, S.B. Ogale, B. Liu, D. Viehland, V. Vaithyanathan, D.G. Schlom, U. V Waghmare, N.A. Spaldin, K.M. Rabe, M. Wuttig, R. Ramesh, Science (New York, N.Y.) 299(5613) (2003) 1719. [8]

- W. Eerenstein, N.D. Mathur, J.F. Scott, *Nature* 442(7104) (2006) 759. [9]
- J. Ma, J. Hu, Z. Li, C.-W. Nan, *Advanced Materials* 23(9) (2011) 1062. [10]
- H. Maleki, M. Haselpour, R. Fathi, *Journal of Materials Science: Materials in Electronics* 29(5) (2018) 4320. [11]
- A. Sarkar, G.G. Khan, A. Chaudhuri, A. Das, K. Mandal, *Applied Physics Letters* 108(3) (2016) 33112. [12]
- S.K. Mandal, T. Rakshit, S.K. Ray, S.K. Mishra, P.S.R. Krishna, A. Chandra, *Journal of Physics: Condensed Matter* 25(5) (2013) 55303. [13]
- Y. Bai, T. Siponkoski, J. Peräntie, H. Jantunen, J. Juuti, *Applied Physics Letters* 110(6) (2017) 63903. [14]
- P.P. Biswas, T. Chinthakuntla, D. Duraisamy, G. Nambi Venkatesan, S. Venkatachalam, P. Murugavel, *Applied Physics Letters* 110(19) (2017) 192906. [15]
- G. Catalan, J.F. Scott, *Advanced Materials* 21(24) (2009) 2463. [16]
- D. Wang, M. Wang, F. Liu, Y. Cui, Q. Zhao, H. Sun, H. Jin, M. Cao, *Ceramics International* 41(7) (2015) 8768. [17]
- H. Fki, M. Koubaa, L. Sicard, W. Cheikhrouhou-Koubaa, A. Cheikhrouhou, S. Ammar-Merah, *Ceramics International* 43(5) (2017) 4139. [18]
- G.A. Smolenskii, V.A. Bokov, *Journal of Applied Physics* 35(3) (1964) 915. [19]
- P. Fischer, M. Polomska, I. Sosnowska, M. Szymanski, *Journal of Physics C: Solid State Physics* 13(10) (1980) 1931. [20]
- I. Sosnowska, T.P. Neumaier, E. Steichele, *Journal of Physics C: Solid State Physics* 15(23) (1982) 4835. [21]
- J.M. Moreau, C. Michel, R. Gerson, W.J. James, *Journal of Physics and Chemistry of Solids* 32(6) (1971) 1315. [22]
- R.T. Smith, G.D. Achenbach, R. Gerson, W.J. James, *Journal of Applied Physics* 39(1) (1968) 70. [23]
- C. Ederer, N.A. Spaldin, *Physical Review B* 71(6) (2005) 60401. [24]

- D. Sando, A. Barthélémy, M. Bibes, *Journal of Physics: Condensed Matter* 26(47) [25]
(2014) 473201.
- J.T. Heron, D.G. Schlom, R. Ramesh, *Applied Physics Reviews* 1(2) (2014) 21303. [26]
- F. Huang, X. Lu, W. Lin, X. Wu, Y. Kan, J. Zhu, *Applied Physics Letters* 89(24) [27]
(2006) 242914.
- Y.P. Wang, L. Zhou, M.F. Zhang, X.Y. Chen, J.-M. Liu, Z.G. Liu, *Applied Physics* [28]
Letters 84(10) (2004) 1731.
- J.-H. Xu, H. Ke, D.-C. Jia, W. Wang, Y. Zhou, *Journal of Alloys and Compounds* [29]
472(1–2) (2009) 473.
- J.B. Neaton, C. Ederer, U. V. Waghmare, N.A. Spaldin, K.M. Rabe, *Physical Review* [30]
B 71(1) (2005) 14113.
- T. Zhao, A. Scholl, F. Zavaliche, K. Lee, M. Barry, A. Doran, M.P. Cruz, Y.H. Chu, [31]
C. Ederer, N.A. Spaldin, R.R. Das, D.M. Kim, S.H. Baek, C.B. Eom, R. Ramesh,
Nature Materials 5(10) (2006) 823.
- D. Lebeugle, D. Colson, A. Forget, M. Viret, P. Bonville, J.F. Marucco, S. Fusil, [32]
Physical Review B 76(2) (2007) 24116.
- R. Safi, H. Shokrollahi, *Progress in Solid State Chemistry* 40(1–2) (2012) 6. [33]
- J. Silva, A. Reyes, H. Esparza, H. Camacho, L. Fuentes, *Integrated Ferroelectrics* [34]
126(1) (2011) 47.
- D. Varshney, A. Kumar, K. Verma, *Journal of Alloys and Compounds* 509(33) (2011) [35]
8421.
- H. Singh, K.L. Yadav, *Journal of Physics: Condensed Matter* 23(38) (2011) 385901. [36]
- Y.-H. Lee, J.-M. Wu, C.-H. Lai, *Applied Physics Letters* 88(4) (2006) 42903. [37]
- F.Z. Li, H.W. Zheng, M.S. Zhu, X.A. Zhang, G.L. Yuan, Z.S. Xie, X.H. Li, G.T. Yue, [38]
W.F. Zhang, *J. Mater. Chem. C* 5(40) (2017) 10615.
- T. Durga Rao, S. Asthana, *Journal of Applied Physics* 116(16) (2014) 164102. [39]
- X. Qi, J. Dho, R. Tomov, M.G. Blamire, J.L. MacManus-Driscoll, *Applied Physics* [40]
Letters 86(6) (2005) 62903.

- X. Zhang, Y. Sui, X. Wang, Y. Wang, Z. Wang, *Journal of Alloys and Compounds* [41]
507(1) (2010) 157.
- Q.R. Yao, Y.H. Shen, P.C. Yang, H.Y. Zhou, G.H. Rao, Z.M. Wang, J.Q. Deng, [42]
Ceramics International 42(5) (2016) 6100.
- B. Yotburut, P. Thongbai, T. Yamwong, S. Maensiri, *Ceramics International* 43(7) [43]
(2017) 5616.
- M. Rangi, S. Sanghi, S. Jangra, K. Kaswan, S. Khasa, A. Agarwal, *Ceramics* [44]
International 43(15) (2017) 12095.
- R. Guo, L. Fang, W. Dong, F. Zheng, M. Shen, *The Journal of Physical Chemistry C* [45]
114(49) (2010) 21390.
- Y. Zhang, A.M. Schultz, P.A. Salvador, G.S. Rohrer, *Journal of Materials Chemistry* [46]
21(12) (2011) 4168.
- H. Maleki, S. Zare, R. Fathi, *Journal of Superconductivity and Novel Magnetism* [47]
(2017) 1.
- H. Maleki, S. Falahatnezhad, M. Taraz, *Journal of Superconductivity and Novel* [48]
Magnetism (2018) 1.
- A. Brisdon, *Applied Organometallic Chemistry* 24(6) (2010) n/a. [49]
- T. Gholam, A. Ablat, M. Mamat, R. Wu, A. Aimidula, M.A. Bake, L. Zheng, J. [50]
Wang, H. Qian, R. Wu, K. Ibrahim, *Journal of Alloys and Compounds* 710 (2017) 843.
- X. Yang, G. Xu, Z. Ren, X. Wei, C. Chao, S. Gong, G. Shen, G. Han, *CrystEngComm* [51]
16(20) (2014) 4176.
- S. Karimi, I.M. Reaney, I. Levin, I. Sterianou, *Applied Physics Letters* 94(11) (2009) [52]
112903.
- J. Tauc, *Materials Research Bulletin* 5(8) (1970) 721. [53]
- † X. H. Wang, † J.-G. Li, †,‡ H. Kamiyama, ‡ and Y. Moriyoshi, † T. Ishigaki*, [54]
(2006).